

Mechanochemical Synthesis and Characterization of Nanostructured ErB_4 and NdB_4 Rare-Earth Tetraborides

Burçak Boztemur,* Faruk Kaya, Bora Derin, Mustafa Lütü Öveçoğlu, Ju Li, and Duygu Ağaoğulları*

Rare-earth borides have become very popular in recent decades with high mechanical strength, melting point, good corrosion, wear, and magnetic behavior. However, the production of these borides is very challenging and unique. The production of ErB_4 and NdB_4 nanopowders via mechanochemical synthesis (MCS) is reported in this study first time in the literature. Er_2O_3 or Nd_2O_3 , B_2O_3 , and Mg initial powders are mechanically alloyed for different milling times to optimize the process. Rare-earth borides with MgO phases are synthesized, then MgO is removed with HCl acid. The nanostructured rare-earth tetraboride powders are analyzed using X-ray diffraction (XRD). Based on the XRD, ErB_4 powders are produced successfully at the end of the 5 h milling. However, the NdB_4 phase does not occur as the stoichiometric ratio, so the B_2O_3 amount is decreased to nearly 35 wt%. When the amount of B_2O_3 is decreased to 20 wt%, NdB_4 and NdB_6 phases are 50:50 according to the Rietveld analysis. However, a homogenous NdB_4 phase is obtained with 30 wt% loss of B_2O_3 . The average particle sizes of ErB_4 and NdB_4 powders are nearly 100.4 and 85.6 nm, respectively. The rare-earth tetraborides exhibit antiferromagnetic-to-paramagnetic-like phase transitions at 18 and 8.53 K, respectively.

including low work function, superconductivity, magnetic properties, thermal electron emission, and narrow-band semiconductor behavior.^[2–4] As a new development, exciting magnetic and electronic physical properties have been found in the RE boride compounds.^[3,5] REB_2 , REB_4 , RE_2B_5 , REB_{12} , REB_6 , and REB_{66} are the main phases of RE, and boron elements. RE borides, such as SmB_6 , PmB_6 , NdB_6 , and EuB_6 , are interesting materials due to their possible uses in quantum computing and electronics.^[6] Also, doping of RE borides has become a popular issue in recent years, with researchers looking into the impact of various dopants on their electrical and magnetic properties.^[7–10] Furthermore, the development of high-entropy RE hexaborides/tetraborides ($\text{HEREB}_6/\text{HEREB}_4$) composite ceramics is a promising field for the study for high-performance electromagnetic wave-absorbing materials.^[11–13]

1. Introduction

Rare-earth (RE) borides which are a family of high-temperature materials have extremely fascinating structural and chemical properties.^[1–3] The combination of boron and metal atoms has significant and thoroughly studied features. Thanks to the particularly strong covalent bonding of boron, great stability and high hardness in extreme conditions are observed for this material type. They exhibit a wide range of physical properties and possible uses,

RE tetraborides received high attention through these materials due to their high melting point, high mechanical strength, high hardness, good chemical stability, and low work function.^[14,15] REB_4 compounds are hard and refractory, making them ideal for coatings on cutting tools, turbine blades, and other high-wear components.^[16] They also have superior thermal conductivity and resistance to oxidation, making them suitable for high-temperature applications.^[17] RE tetraborides have a tetragonal crystal structure with a space group $\text{P4}/\text{mbm}-\text{D}_{4h}^{18}$. REB_4


B. Boztemur, M. L. Öveçoğlu, D. Ağaoğulları
 Faculty of Chemical and Metallurgical Engineering
 Department of Metallurgical and Materials Engineering
 Particulate Materials Laboratories (PML)
 Graphene & 2D Materials Laboratory
 Istanbul Technical University
 Maslak, Istanbul 34469, Türkiye
 E-mail: boztemur15@itu.edu.tr; bozkurtdu@itu.edu.tr

F. Kaya, B. Derin
 Faculty of Chemical and Metallurgical Engineering
 Department of Metallurgical and Materials Engineering
 Istanbul Technical University
 Maslak, Istanbul 34469, Türkiye

M. L. Öveçoğlu
 Department of Mechanical Engineering
 MEF University
 Maslak, Istanbul 34396, Türkiye

J. Li
 Department of Materials Science and Engineering
 Massachusetts Institute of Technology
 77 Massachusetts Avenue, Cambridge, MA 02139, USA

J. Li
 Department of Nuclear Science and Engineering
 Massachusetts Institute of Technology
 77 Massachusetts Avenue, Cambridge, MA 02139, USA

 The ORCID identification number(s) for the author(s) of this article can be found under <https://doi.org/10.1002/adem.202400842>.

© 2024 The Author(s). Advanced Engineering Materials published by Wiley-VCH GmbH. This is an open access article under the terms of the Creative Commons Attribution-NonCommercial-NoDerivs License, which permits use and distribution in any medium, provided the original work is properly cited, the use is non-commercial and no modifications or adaptations are made.

DOI: 10.1002/adem.202400842

compounds exhibit metallic properties and order antiferromagnetically, but only PrB_4 orders ferromagnetically.^[19,20] There are many magnetic interactions in the REB_4 structure competing with the direct exchange such as the indirect exchange between conduction electrons (Ruderman–Kittel–Kasuya–Yosida type), crystal electric field, magnetoelastic coupling, and quadrupolar interactions.^[8,21] Furthermore, putting these magnetic moments in a specific crystal structure such as $\text{P4}/\text{mbm}-\text{D}_{5h}^{54}$ will result in a complex frustrated magnetic system, particularly one formed by the RE tetraborides (REB_4), where all interactions between adjacent spins cannot be satisfied at the same time, suppressing magnetic order and resulting in ground state degradation, that is, the formation of several different magnetic states with the same energy.^[22,23]

Based on the ErB_4 and NdB_4 production methods, there are few examples in the literature. However, there is not any example about mechanochemical synthesis (MCS) of REB_4 . The RE tetraboride powders were produced by MCS from low-cost Er_2O_3 , Nd_2O_3 , B_2O_3 , and Mg initial powders for the first time. This method is a novel, simple, and room-temperature process that enables control of the product microstructure (phase, shape, size, etc.) and obtaining homogeneous materials. Thanks to these advantages, ErB_4 and NdB_4 powders were produced with high quality and at nanoscale. A thorough analysis was conducted on the impact of milling duration as a process parameter on the resulting phases. After the synthesis process, a purification treatment with HCl acid was applied to achieve nanostructured ErB_4 and NdB_4 powders. Also, different characterization methods such as XRD, particle size analyses, scanning electron microscope (SEM), and transmission electron microscope attached with energy-dispersive spectroscopy (EDS) were used for examining the powders. In addition, the RE tetraboride powders were analyzed based on their magnetic properties. Also, it created an excellent area with different magnetic applications.

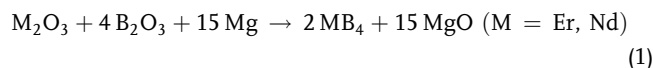
2. Experimental Section

2.1. Raw Materials and Precursor Preparation

Thermochemical modeling (CALPHAD) was performed using FactSage8.3 simulation software^[24] to conduct virtual experiments pertaining to the mechanochemical reactions (Equation (1)). In the simulations, the “equilib” module was utilized under 1 atm and under nonadiabatic ($\Delta H \neq 0$) conditions since the experimental setup is not heat insulated. The “reaction” module was also utilized in order to calculate the ΔH and ΔG of the reactions at 25 °C. The temperature of the reactor was known to be well below the adiabatic temp (≈ 600 °C),^[25] the temperature was set as 600 °C with varying B_2O_3 and Mg input molar concentrations and the thermodynamically possible reaction products were graphed using FactPS, SGTE, and AIMP databases.

Er_2O_3 (ABCR, 99.99% pure), Nd_2O_3 (Alfa Aesar, 99% pure), B_2O_3 (ETI Mine, 98% pure), and Mg powders (MME, 99.7% pure) were the starting materials for mechanical milling. Malvern Mastersizer 2000 particle size analyzer (PSA) was used for measuring the average particle sizes of the Er_2O_3 , Nd_2O_3 ,

B_2O_3 , and Mg starting powders as 9.5 ± 0.05 , $\approx 5 \pm 0.01$, 466.9 ± 0.12 , and 142.7 ± 0.09 μm , respectively. Powder batches that were called as-blended were prepared according to stoichiometry and blended for 2 h in a WAB T2C Turbula mixer in order to provide a homogeneous blend. Stoichiometry for the synthesis of ErB_4 using Er_2O_3 , B_2O_3 , and Mg powders was given by the reduction reaction in Equation (1). The stoichiometric amounts of the initial reactants Er_2O_3 : B_2O_3 : Mg were 2.242 (1 mol): 1.632 (4 moles): 2.136 g (15 moles) for powders as per Equation (1). Also, stoichiometry for the synthesis of NdB_4 from the Nd_2O_3 , B_2O_3 , and Mg powders is given by the reduction reaction in Equation (1). The stoichiometric amounts of the initial reactants Nd_2O_3 : B_2O_3 : Mg were 2.0626 (1 mol): 1.7071 (4 moles): 2.2348 g (15 moles) for powders as per Equation (1).



2.2. Mechanochemical Synthesis and Purification

Prepared as-blended powders and hardened steel balls (6 mm ϕ) were placed to hardened steel vials (50 mL). The ball-to-powder weight ratio was kept constant at 10:1. The most frequent types of materials used for the grinding medium were hardened steel, tool steel, bearing steel, tempered steel, hardened chromium steel, stainless steel, WC \pm Co, alumina, and zirconia.^[26] The reason for choosing hardened steel milling set was that the impurity coming from the media could be removed with an additional purification treatment. Fe or Fe-based impurities can be removed with concentrated acids such as HCl, H_2SO_4 . Sarker et al.^[27] proved that Fe in the RE elements was dissolved with the HCl solution as 100%. The vials that included powders and balls were sealed under argon (Ar) atmosphere (Linde, 99.999% pure) in a MBraun glove box. Then, MCS was conducted on the as-blended powders in a high-energy NanoMultiMix mill at 920 rpm for different durations up to 8 h. The high-energy impacts that caused mechanical deformation in the powder particles provided the necessary energy to start the reaction. After MCS, while the RE borides formation was provided, MgO was the by-product. The selective acid leaching with 4 M HCl solution (HCl, Merck, 37%) was applied to the MCS'ed powders to obtain RE borides under the ultrasonic stirring using a Bandelin Sonorex RK-100H ultrasonic bath. The leaching treatment was conducted at 80 °C for 15 min with a solid-to-liquid ratio of 1 g/10 cm^3 . The residue was then separated from the leaching solution by repeated centrifugation (Hettich Rotofix 32 A, 4000 rpm, 30 min), decantation, and rinsing steps. Repeated centrifugation was arranged to the proper pH value of the solution. When this value reached ≈ 5 , the centrifugation was stopped, and the residue was dried in an FN 500 stove at 120 °C for 24 h in air. Supernatant liquids of the leached product were collected in a volumetric flask and subsequently subjected to chemical analysis to control the contaminants arose from debris of the milling media. From now on, the residue was called as leached powders. **Figure 1** shows the synthesis of ErB_4 and NdB_4 powders by MCS and purification processes.

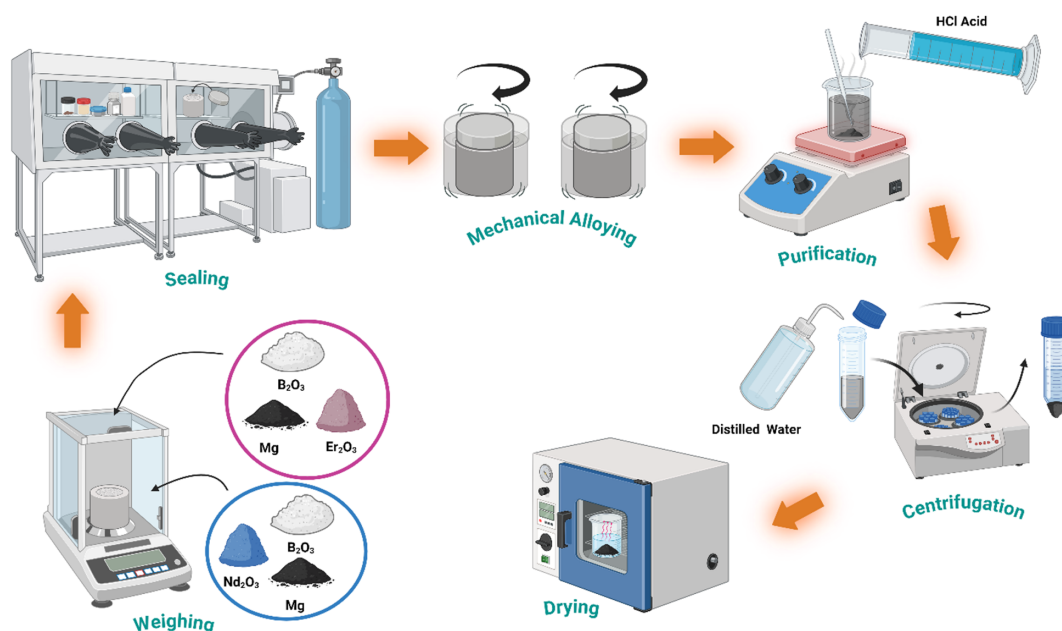


Figure 1. Mechanochemical synthesis and purification process of ErB_4 and NdB_4 production. (created by biorender.com).

2.3. Characterization

The phases of powders that were produced by MCS and leaching were examined with XRD method (Bruker D8 Advanced Series X-ray powder diffractometer with $\text{CuK}\alpha$ ($\lambda = 0.154 \text{ nm}$, 40 kV and 40 mA)) in the 2θ range of 10° – 90° incremented at a step size of 0.02° at a rate of 2° min^{-1} . Then, the crystal structure and lattice parameter(s) of the crystalline phases were analyzed using the International Center for Diffraction Data (ICDD) powder diffraction files. The average crystallite sizes and lattice strains of the MCS'ed ErB_4 and NdB_4 powders were measured with the modified Scherrer's formula using Bruker-AXS TOPAS V3.0 software.^[28] The five peaks of ErB_4 phase in $22.21^\circ/(001)$, $25.17^\circ/(020)$, $28.20^\circ/(120)$, $33.81^\circ/(111)$, $36.18^\circ/(021)$, and NdB_4 phase in $21.82^\circ/(001)$, $24.85^\circ/(020)$, $27.77^\circ/(120)$, $33.20^\circ/(111)$, $35.54^\circ/(021)$ degrees and planes were taken for average crystallite size and lattice strain calculations. The amounts of the different phases in the XRD of MCS'ed NdB_4 powders were identified by the semi-quantitative Rietveld method. A Microtrac Nano-flex PSA equipped with a Bandelin Sonopuls ultrasonic homogenizer was used for measuring powder particle sizes in the alcohol media. The density of the leached powders was measured using a Micromeritics AccuPycII 1340 gas pycnometer in a 1 cm^3 sample chamber at room temperature using He gas (Linde, 99.996% pure) as the displacement medium. The microstructural characteristics of the MCS'ed powders (dropped onto a carbon tape) were examined with a Thermo Scientific Quattro S SEM equipped with an EDS. EDS results were reported as the arithmetic means of three different measurements taken from the same regions in the samples. The specimens were investigated by JEOL JEM 2100 high-resolution transmission electron microscope (TEM, LaB_6 filament) operated at 200 kV and equipped with an Oxford Instruments X-Max 80T EDS system.

Lacey Carbon film on 200 mesh copper TEM grids (Electron Microscopy Sciences, LC200-Cu, 200 mesh) was used. Images were taken by Gatan Model 833 Orius SC200D CCD Camera. High-magnification images were taken by Gatan Model 794 Slow Scan CCD Camera. Gatan Microscopy Suite (GMS) 2 software was used. The selected area electron diffraction (SAED) patterns were taken for analysing phases. Also, the average size of nearly 100 particles was measured in the TEM. Additionally, probable contaminants released from the milling media such as Fe, Cr, Ni elements were analyzed in the supernatant liquids using a PerkinElmer 1100B Atomic Absorption Spectrometer (AAS). The supernatant liquids after leaching were diluted with distilled water based on the device reading limit ($\approx 1/1000$ dilution). Then, filter paper was used to pour stock solution before every measurement to remove suspended particles. The results were multiplied with a diluted factor for obtaining final results. A Quantum Design MPMS3 superconducting quantum interference device magnetometer was used for magnetic measurements under an applied field of 200 Oe. Moreover, Bruker Alpha-II Fourier-transform infrared spectroscopy (FTIR) was used in order to understand B–O bonding.

3. Results and Discussions

3.1. Thermochemical Simulations

According to the calculations in the “reaction” module, the ΔH and ΔG of the reactions at 25°C were found to be -3371.3 and $-3229.4 \text{ kJ mol}^{-1}$ for the $\text{NdB}_4 + \text{NdB}_6$ synthesis reaction and -2578.4 and $-2504.0 \text{ kJ mol}^{-1}$ for the ErB_4 synthesis reaction (Equation (1)), respectively. These values demonstrate the exothermic nature of the mechanochemical redox reactions. Based on these MCS reactions, the equilibrium module

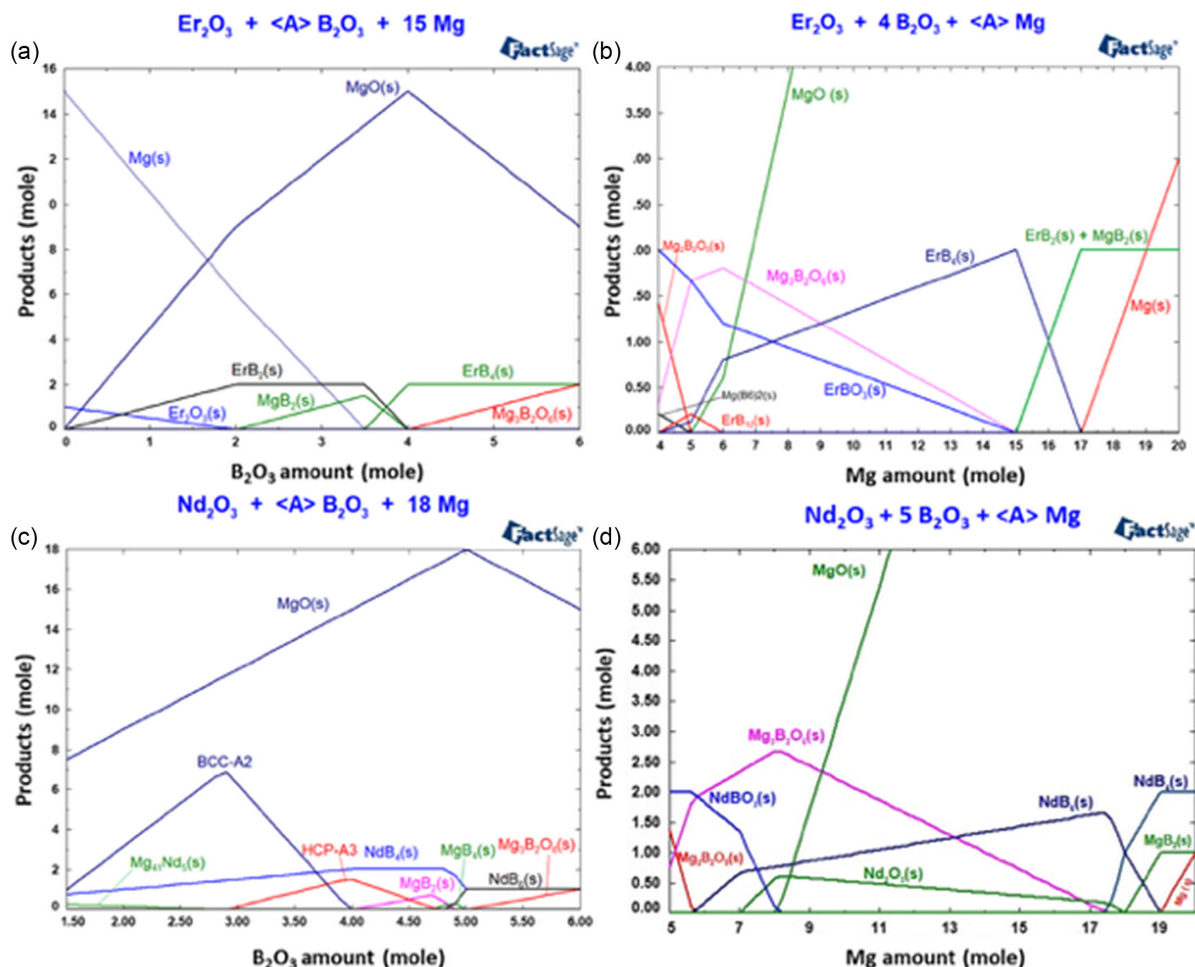


Figure 2. Thermochemical simulation of the reaction products for the stoichiometric powder blend, the effect of varying B_2O_3 and Mg contents at a fixed temperature of 600 °C for the a,b) Erbium and c,d) Neodymium boride setups.

calculations show that for the ErB_4 system (Figure 2a,b), at stoichiometric conditions (shown in the dotted red line), the reaction products were ErB_4 and MgO . Under B_2O_3 lean conditions with stoichiometric Mg (15 moles), it was possible to obtain ErB_2 together with MgB_2 . When the B_2O_3 content increased, the reaction resulted in a boron-enriched ErB_4 phase, and excess B_2O_3 reacted with by-product MgO and started to form the $\text{Mg}_3\text{B}_2\text{O}_6$ phase. Mg lean condition (Figure 2b) might result in the formation of ErBO_3 and $\text{Mg}_3\text{B}_2\text{O}_6$, which causes inefficient synthesis for the ErB_4 powders. There is also the possibility of the formation of ErB_{12} when the Mg content is below 6 moles. Excess Mg beyond the stoichiometric amount (15 moles), on the other hand (Figure 2b), might cause the formation of ErB_2 and MgB_2 mixture. NdB_4 synthesis simulations were similar to that of the ErB_4 since their chemical properties are similar. The $\text{NdB}_6 + \text{NdB}_4$ mixture ($\text{NdB}_{4.6}$) is found to be similar to our earlier calculations as well.^[25] B_2O_3 lean conditions below the stoichiometry (5 moles) might cause the formation of NdB_4 -rich mixtures together with magnesium borides (MgB_2 , MgB_4). On the other hand, as B_2O_3 increases, an equimolar NdB_4 and NdB_6 mixture could be obtained; further increment results,

again, in the formation of $\text{Mg}_3\text{B}_2\text{O}_6$, similar to the ErB_4 system. Mg lean conditions (Figure 2d) for the neodymium system, when the B_2O_3 is fixed at the stoichiometric amount (5 moles), increases the NdB_4 content, which is 50:50 at the stoichiometric Mg amount (18 moles). Excess Mg, on the other hand, increases NdB_4 back again due to the formation of MgB_2 . The CALPHAD simulations indicate that it is thermodynamically feasible to produce mixtures of ErB_4 , NdB_4 , and $\text{NdB}_{4.6}$ within the experimental conditions employed. These mixtures can be purified by dissolving the MgO by-product through leaching in an HCl solution.

3.2. Characterization of ErB_4 and NdB_4 Powders

Er_2O_3 , B_2O_3 , and Mg powders were mechanochemically synthesized for up to 8 h to produce ErB_4 nanopowders. Figure 3a shows the XRD patterns of the as-blended Er_2O_3 , B_2O_3 , and Mg powders and those mechanically milled for different durations up to 4 h. In the XRD pattern of the as-blended (nonmilled) powders, Er_2O_3 (ICDD Card No: 03-065-3175, Bravais lattice: primitive cubic, $a = 1.053 \text{ nm}$), Mg (ICDD Card No: 00-035-0821,

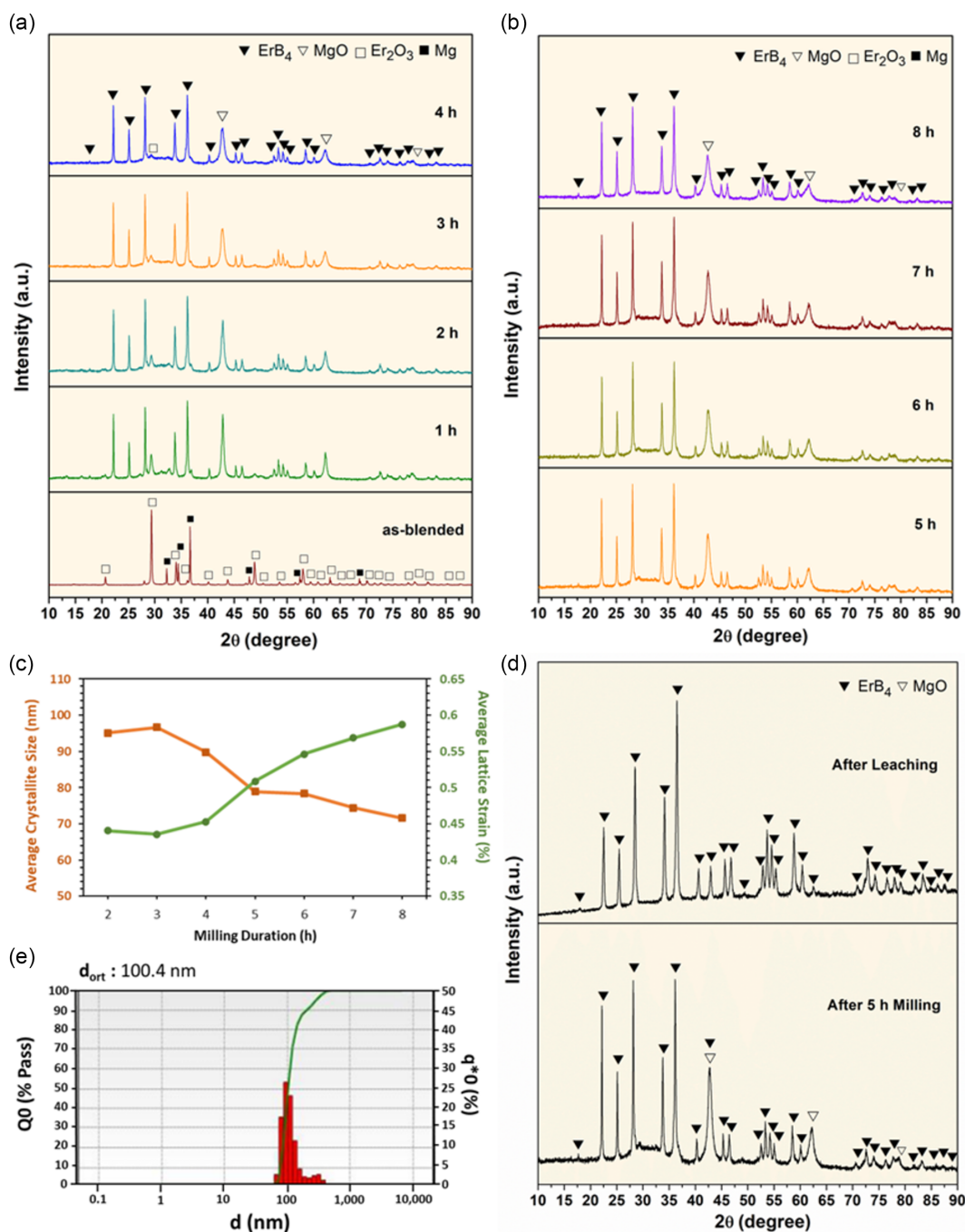


Figure 3. XRD patterns of the a,b) as-blended, 1-4 h, and 5-8 h MCS'ed Er₂O₃, B₂O₃, and Mg powders, c) the average crystallite size and lattice strain of ErB₄ phase versus milling duration, d) 5 h MCS'ed and 4 M HCl leached ErB₄-MgO powders, and e) the average particle size of ErB₄ powders.

Bravais lattice: primitive hexagonal, $a = 0.321$ nm and $c = 0.521$ nm) phases were detected. The characteristic peaks of B₂O₃ were not observed in the XRD pattern of the as-blended powders because of their amorphous nature. After 1 h of milling of the powders, MgO (ICDD Card No: 00-045-0946, Bravais lattice: face-centered cubic, $a = 0.422$ nm) and ErB₄ (ICDD Card No: 01-089-3552, Bravais lattice: tetragonal, $a = 0.701$ nm and $c = 0.404$ nm) phases were observed. However, the Er₂O₃ phase

was still in the structure. Therefore, 1 h milling duration can be considered as the initial point for the formation of the boride phases. At the end of 4 h milling, the only detected phases were ErB₄ and MgO. Based on the XRD patterns (Figure 3b), there were no changes after 5 h milling up to 8 h. Figure 3c illustrates the average crystallite sizes and lattice strains of the mechanically alloyed powders up to 8 h for ErB₄ phases. On the basis of the related XRD patterns, the average crystallite sizes of the ErB₄ phase in the

powders milled for between 2 and 8 h were calculated as 89.8, 96.67, 89.83, 78.9, 78.33, 74.4, and 71.6 nm, respectively. Furthermore, the average lattice strains of the ErB_4 phase were calculated as 0.431, 0.441, 0.436, 0.453, 0.556, 0.546, 0.569, and 0.588% for the 2 and 8 h milling. Extending the milling duration to 5 h did not change the nature of the resulting products: ErB_4 and MgO phases were still present in the 5 h milled powders and no new phases formed. The reaction in Equation (1) completely took place after MCS that was conducted by 5 h milling, and the optimum time was chosen as 5 h for the purification. XRD patterns of the ErB_4 phase after 5 h milling and 4 M HCl leaching contained 27 peaks which are consistent with the standard ErB_4 pattern as shown in Figure 3d. ErB_4 pattern had 22 peaks (17.73, 22.21, 25.17, 28.20, 33.81, 36.18, 40.30, 42.61, 45.31, 46.49, 53.38, 54.22, 55.06, 58.51, 60.09, 62.23, 70.59, 72.55, 73.97, 76.26, 77.65, 78.88°). As clearly seen, the acid concentration was sufficient

to completely remove the MgO phase from the powders, and any impurity was not observed in 4 M leaching. Moreover, the average crystallite size and lattice strain of the leached powders were determined as 94.64 nm and 0.228% according to the XRD pattern. In addition, the PSA graph of the leached ErB_4 powders as given in Figure 3e illustrates that the average particle size of the ErB_4 was about 100.4 nm. Moreover, the lognormal distribution type was observed for this graph. The pycnometer density of the purified ErB_4 powders were measured as $6.15 \pm 0.015 \text{ g cm}^{-3}$. In the literature, there is not too much information about the production of ErB_4 . In one study, Novikov et al.^[18] reported that the polycrystal of ErB_4 was produced with the borothermal reduction of metal from its oxide in a vacuum (5×10^{-5} Torr, 1750 °C, and 2.5 h). These RE borides can be produced with shorter time and less energy via MCS. **Figure 4** shows SEM ($\times 60\,000$, and $120\,000$ magnifications) and TEM ($1\,\mu\text{m}$ and $500\,\text{nm}$ scales) images, particle size

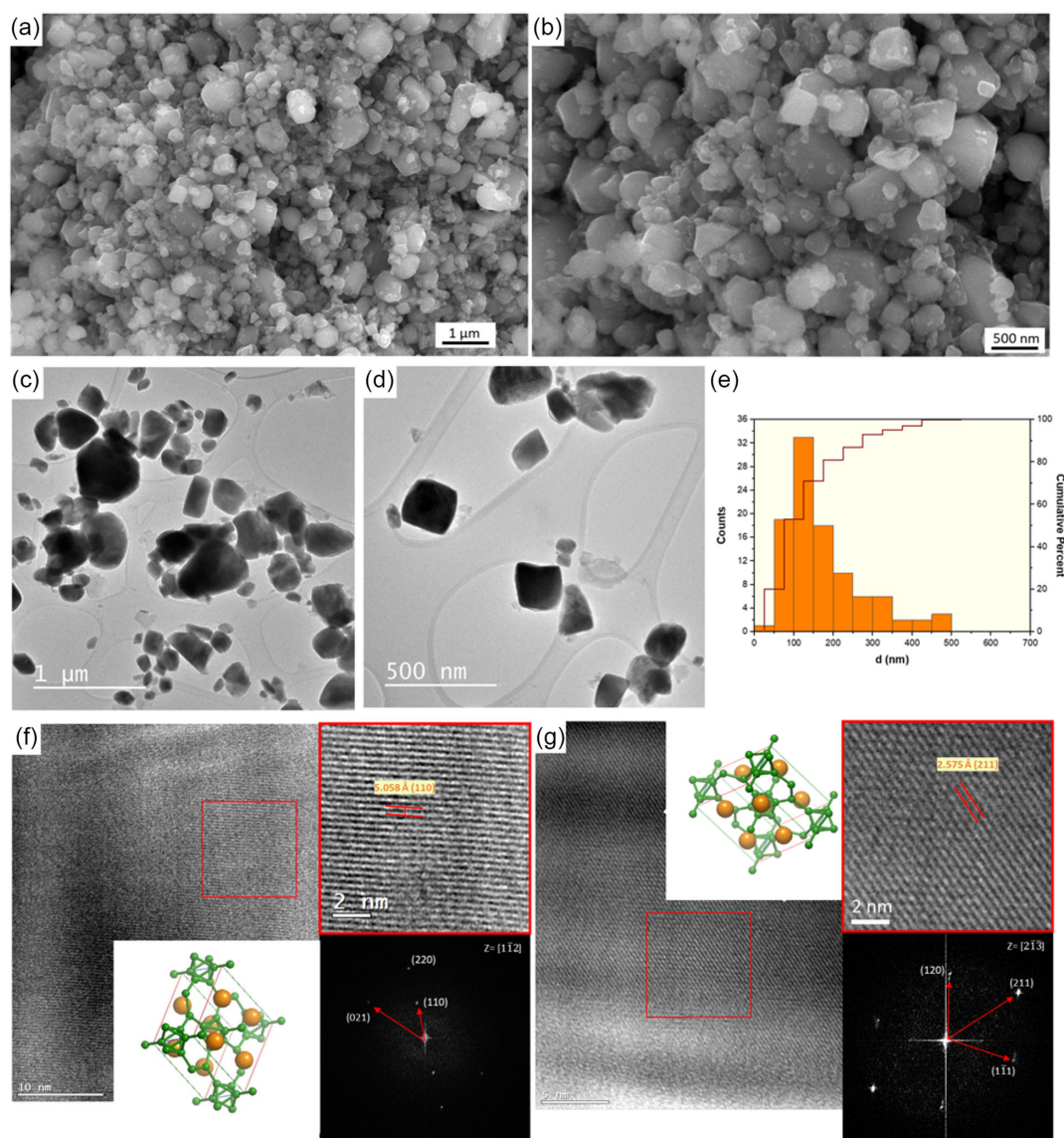


Figure 4. a,b) SEM, c,d) TEM images with different magnifications, e) particle size measurements from TEM image, and f,g) SAED images with the interplanar distance calculations and atomic structure of ErB_4 nanopowders.

measurement based on the TEM image, and the interplanar distance measurements with SAED pattern. According to the SEM and TEM images, the shape of ErB_4 particles was nearly mixed morphology. According to the particle size measurements from the TEM image (Figure 4c), it can be understood that ErB_4 particles ranged between 100 and 150 nm, and this result matched with the particle size analysis (Figure 4e). The general EDS analysis taken from Figure 4 revealed the presence of Er, and B elements. Also, the amount of Er and B elements was measured at 70.8% and 29.2% as atomic percentages. The interplanar distance was measured as 5.058 Å, and this value belongs to (110) plane for ErB_4 phase. Also, (021) and (110) planes were detected from $[1\bar{1}2]$ zone axis in the SAED pattern (Figure 4f). In addition to that, a different area showed that the interplanar distance was measured as 2.575 Å for the (211) plane. Based on the $[2\bar{1}\bar{3}]$ zone axis, (211), (120), and $(1\bar{1}1)$ planes were detected in the SAED pattern (Figure 4g). In the literature, Ağaoğlu et al.^[29,30] showed that the amounts of Fe, Ni, and Cr were nearly 7–11, 0.2, and 1.2 ppm, respectively, with

the same production method for the RE borides. In this study, 14 ppm Fe, 0.95 ppm Cr, and 0.3 ppm Ni were detected based on the AAS results. These results were very close to the literature and showed that the impurity may be removed with acid leaching down to a detection limit. It should be also noted that any detection of impurity down to a ppb level was not conducted on the powders in this study.

In our previous study, NdB_6 powders were produced with MCS from Nd_2O_3 , Mg, and B_2O_3 raw materials.^[25] In this study, NdB_4 production from Nd_2O_3 , Mg, and B_2O_3 initial powders with 920 rpm MCS for 5 h was aimed. Figure 5 shows the XRD patterns and Rietveld analysis of $\text{NdB}_{4,6}$ and NdB_4 powders. The little amounts of NdB_4 phase were observed as this stoichiometric amount. So, B_2O_3 amount was decreased and it was named as 5–35 wt% B_2O_3 loss. B_2O_3 was decreased about by 20 and 30 wt% amount in the stoichiometric powder batch (Figure 5a). Reactant and product amounts with milling conditions for NdB_4 production are shown in Table S1. Figure 5b,c shows that while the

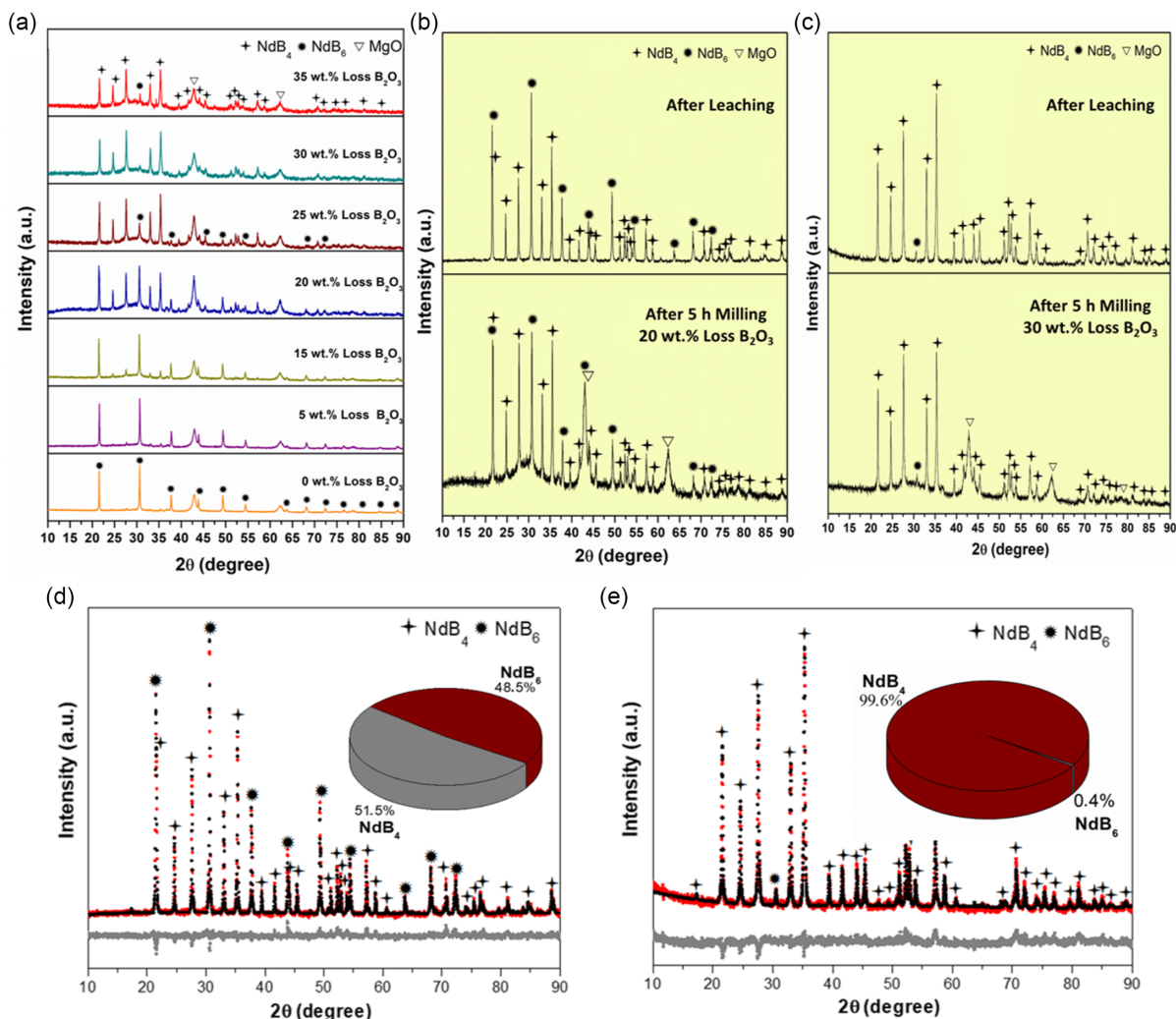


Figure 5. XRD patterns of the a) NdB_4 , NdB_6 , and MgO phases with 920 rpm MCS for 5 h with decreasing amount of B_2O_3 , ErB_4 production with b) loss of 20 wt% B_2O_3 , c) loss of 30 wt% B_2O_3 after 5 h and 4 M HCl leaching, and Rietveld analysis of d) $\text{NdB}_{4,6}$ powders, R_p : 4.5, R_{wp} : 5.79, GoF: 1.41, R_{Bragg} of NdB_4 : 4.86 and R_{Bragg} of NdB_6 : 3.02. e) NdB_4 powders, R_p : 4.94, R_{wp} : 6.17, GoF: 1.68, R_{Bragg} of NdB_4 : 4.62 and R_{Bragg} of NdB_6 : 3.69.

B_2O_3 amount decreased to nearly 20 wt%, $NdB_{4.6}$ phase was observed. It means that nearly 50 wt% NdB_4 and 50 wt% NdB_6 phases were simultaneously in the same structure. However, when the B_2O_3 amount decreased to 30 wt% amount, a homogenous NdB_4 phase was determined. After MCS, NdB_4 and $NdB_{4.6}$ powders were leached with 4 M HCl. XRD patterns of NdB_4 phase had 21 peaks with these values of 21.82° , 24.85° , 27.77° , 33.20° , 35.54° , 39.62° , 41.83° , 44.28° , 45.62° , 51.38° ,

52.39° , 53.01° , 54.02° , 57.36° , 58.89° , 70.84° , 72.22° , 74.27° , 75.58° , 77.18° , and 81.25° . Rietveld analysis of NdB_4 and $NdB_{4.6}$ are given in Figure 5d,e. The amounts of NdB_6 and NdB_4 were approximately calculated at 49 and 51 wt%, respectively. Lattice parameters of NdB_6 and NdB_4 were calculated as a : 0.413 nm (cubic), a : 0.721 nm, c : 0.410 nm (tetragonal), respectively. According to the Rietveld analysis, while the amount of NdB_6 was nearly 0.4 wt%, it was 99.6 wt% NdB_4 for the 20 wt%

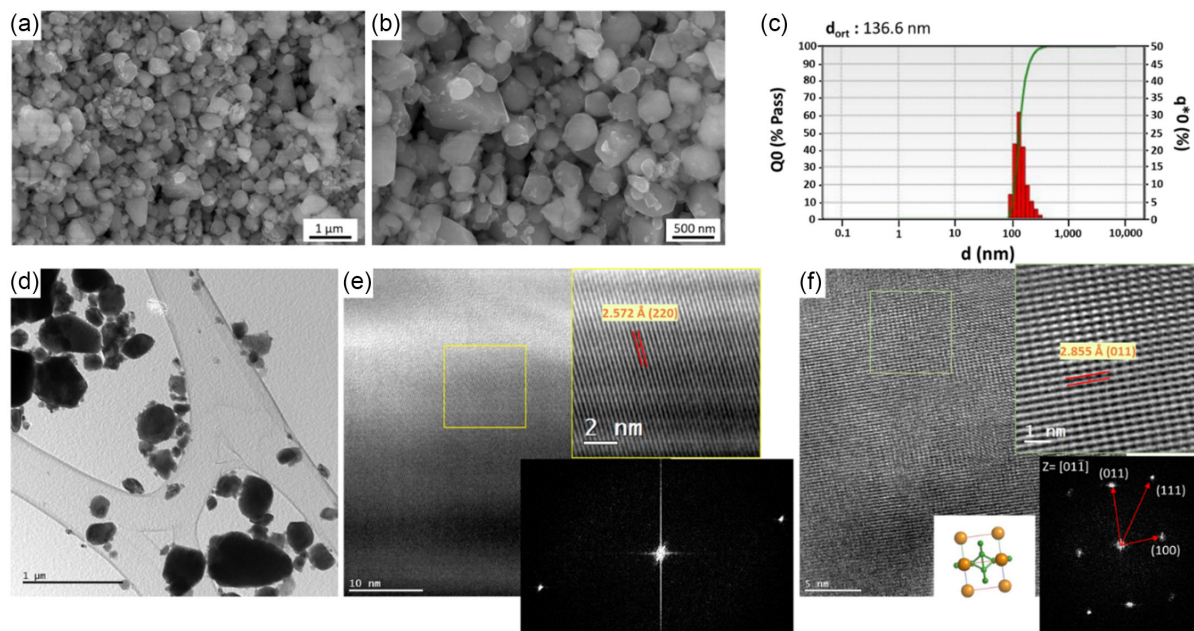


Figure 6. a,b) SEM images at $\times 60\,000$ and $120\,000$ magnifications, c) average particle size analysis, and d–f) TEM and SAED images with interplanar distance and plane calculations of $NdB_{4.6}$.

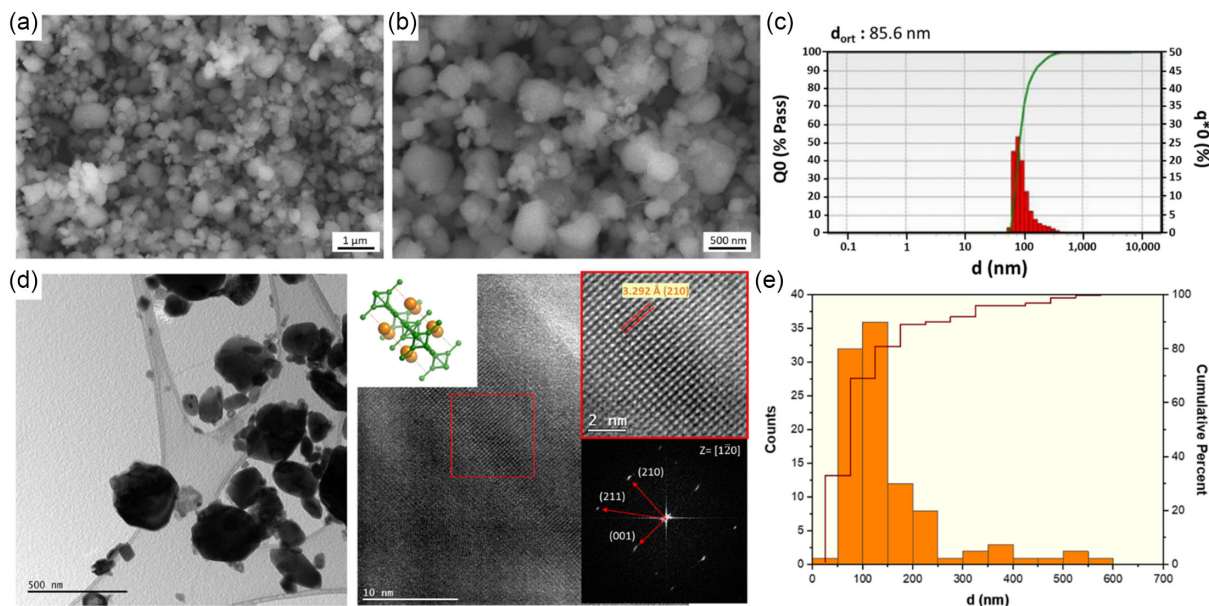


Figure 7. a,b) SEM images ($\times 60\,000$ and $120\,000$), c) average particle size analysis, d) TEM and SAED images with interplanar distance and plane calculations, and e) particle size measurements from TEM images of NdB_4 nanopowders.

loss B_2O_3 . Lattice parameters of NdB_4 were calculated as a : 0.721 nm and c : 0.410 nm. These values were nearly the same with the lattice parameter taken from PDF cards. In the literature, there is only one study for the production of NdB_4 . Salamakha et al.^[31] studied that arc melting method was used for the production of single-crystal NdB_4 . In this study, NdB_4 and $NdB_{4.6}$ powders were produced with low cost and nanoscale.

Figure 6 and **7** displays SEM and TEM images at various magnifications and the average particle size and interplanar distance measurements of the $NdB_{4.6}$ and NdB_4 powders. Powder morphology and form were almost identical and mixed for the all powders. A higher magnification of the SEM image showed that the $NdB_{4.6}$ and NdB_4 particle sizes were between almost 80 and

120 nm. Additionally, the particle size analysis graph in **Figure 6** and **7c** shows that the $NdB_{4.6}$ and NdB_4 average particle size was ≈ 136.6 and 85.6 nm, respectively, which is in the same range as seen in the SEM image. For this graph, a lognormal distribution type was seen. Furthermore, the density of $NdB_{4.6}$ and NdB_4 powders was determined to be 4.09 ± 0.004 and 5.02 ± 0.011 g cm⁻³. It can be understood that the density of powders increased with decreasing boron amount. Boztemur et al.^[25] mentioned that the density of NdB_6 was nearly 4.03 ± 0.01 g cm⁻³. In the TEM calculations, the interplanar distance which is 2.572 Å belongs to (220) plane which was determined for the NdB_4 phase. Also, based on the $[01\bar{1}]$ zone-axis, (011), (111), and (100) planes were detected for the NdB_6 phase

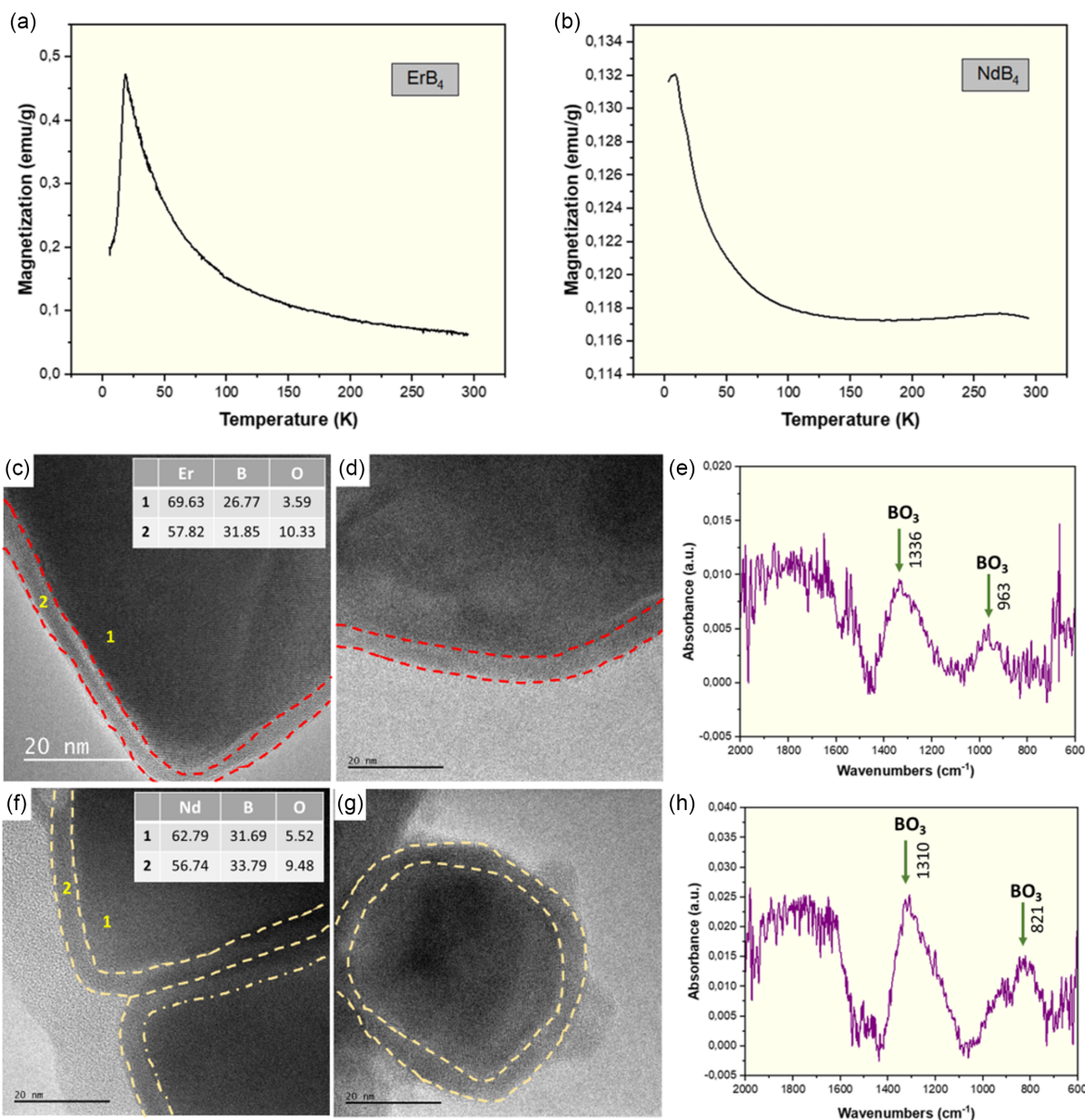


Figure 8. a,b) The magnetization diagrams of the RE tetraborides, TEM images with point EDS results, and FTIR analyses of c–e) ErB_4 and f–h) NdB_4 powders.

in the SAED pattern (Figure 6f). Finally, (210), (211), and (001) planes were detected for the NdB_4 phase in the SAED pattern (Figure 7f) from the $[1\bar{2}0]$ zone axis. According to the AAS results, Fe, Cr, and Ni amounts were measured as 11, 0.98, and 0.28 ppm, respectively, for the $\text{NdB}_{4.6}$ powders. Additionally, these values changed to 12 ppm of Fe, 0.92 ppm of Cr, and 0.23 ppm of Ni for the NdB_4 sample. These results were very close to the ErB_4 and literature values. The impurity detection in the structure of the powders was not carried out in the ppb level. NdB_6 and NdB_4 phases were observed for the $\text{NdB}_{4.6}$ powders.

NdB_4 and ErB_4 , RE tetraborides, in general, are known to possess interesting and complex magnetic properties such as successive phase transitions, magnetic frustration, ferrimagnetic plateaus, etc. thanks to their unique crystal structure.^[8,20,22,23,32–35] ErB_4 exhibits an antiferromagnetic (AF) transition occurring at $T_{\text{Néel}} = 15.4$ K, where the orientation of its easy axis aligns along the *c* direction, and each Er ion possesses a magnetic moment of $8.2 \mu_{\text{B}}/\text{Er ion}$.^[8,33,35] In Figure 8a,b, considering our sample was in powder form, MCS'ed ErB_4 powders exhibited maximum magnetization of $0.4726 \text{ emu g}^{-1}$ at about $T = 18$ K corresponding more or less similar AF transition temperatures. The magnetization decreases with a paramagnetic behavior as temperature increases. MCS'ed NdB_4 powders on the hand exhibited even lower magnetic moment 0.132 emu g^{-1} with a maximum at about $T_{\text{Néel}} = 8.53$ K which was very close to the AF temperature reported in the literature.^[23,34] Also, if there was Fe impurity in the structure, this value would be expected to be much higher. Since the saturation magnetization, thus magnetic moment per Nd ion as expected from the Hund's rules^[21] ($3.2 \mu_{\text{B}}^{[23]}$), is lower than Er ion, the lower magnetization of NdB_4 than ErB_4 is already expected. In the literature, it is known that the magnetic field necessary to saturate the magnetization for RE tetraborides, such as NdB_4 and ErB_4 ,^[23,32] is on the order of 30–50 kOe, depending on the temperature. Our applied magnetic field is very low (200 Oe) compared to the literature, not enough to saturate the magnetic moments, thus resulting in lower magnetization values. Although magnetization exhibits anisotropy in these tetragonal crystals, the anisotropy is averaged over in our powdered samples. In our previous study for NdB_6 powder, we found that defective crystal structures can be achieved through MCS and leaching methods which can have crucial effects on the magnetic and mechanical properties.^[25] The likely explanation of this may be attributed to the formation of B vacancies and lattice shrinkage. This reduction in lattice size could contribute to a decrease in spin asymmetry, a phenomenon previously demonstrated by our research group.^[25] Thus, any discrepancies in the observed Néel temperatures and magnetization values can be expected to arise from the defected crystals. In addition, the TEM images showed that an amorphous layer exists around some of the particles (Figure 8c,d). These layers included a high amount of RE, boron, and oxygen based on the EDS results. The presence of the oxygen certainly has a negative contribution to the magnetization per gram of the sample, because it is heavier than boron, the RE ions in these amorphous layer can be expected to retain their paramagnetic effective magnetic moment.^[36] Figure 8e,h illustrates the FTIR analyses results for the ErB_4 and NdB_4 nanostructured

powders. The IR absorbance in the $1200\text{--}1500 \text{ cm}^{-1}$ range is assigned to asymmetric stretching of B–O bond in trigonal BO_3 units.^[37] The B–O stretching in tetrahedral BO_4 units is in the range of $800\text{--}1200 \text{ cm}^{-1}$. The bending vibrations of bridging oxygen (B–O–B) between BO_3 and BO_4 units are active in the range of $600\text{--}800 \text{ cm}^{-1}$.^[38–40] In our study, the peak interval of FTIR for ErB_4 and NdB_4 powders was nearly in this range. As supported by the CALPHAD calculations (Figure 2b), under Mg-lean conditions for REB_4 , the presence of REBO_3 was observed. This formation of the amorphous layer around the particles can be attributed to the REBO_3 as supported by the FTIR results which cannot be detected via XRD analyses because of its amorphous structure.

4. Conclusion

In the present study, nanostructured ErB_4 and NdB_4 ceramic powders were successfully prepared through a simple two-step process that includes MCS via high-energy ball milling, followed by purification through HCl leaching. A novel and simple process for synthesizing nanostructured ErB_4 and NdB_4 powders was achieved by the mechanochemical reaction of powder blends containing stoichiometric amounts of $\text{Er}_2\text{O}_3/\text{Nd}_2\text{O}_3$, B_2O_3 and Mg powders. During the mechanochemical processing of $\text{Er}_2\text{O}_3/\text{Nd}_2\text{O}_3$, B_2O_3 and Mg starting powders, the formation of the ErB_4 and NdB_4 phase started only after 1 h of milling. Extending the milling duration to 5 h resulted in the major NdB_4 and MgO phases. Powders milled for 5 h were successfully purified by leaching in 4 M HCl, resulting in the formation of nanostructured ErB_4 and NdB_4 powders with mixed rounded-shape morphology (average size of 100.4 and 85.6 nm) free from undesired MgO. For the production of NdB_4 powders, B_2O_3 amount was decreased from stoichiometric. MCS'ed ErB_4 and NdB_4 powders exhibited maximum magnetization of $0.4726 \text{ emu g}^{-1}$ accompanied with an AF-to-paramagnetic phase transition at about $T_N = 18$ K and 0.132 emu g^{-1} with a maximum at about $T_N = 8.53$ K, respectively. An amorphous layer can be found around the particles which was attributed to the REBO_3 formation based on the FTIR analyses, supported by the CALPHAD calculations.

Supporting Information

Supporting Information is available from the Wiley Online Library or from the author.

Acknowledgements

This study was supported by Istanbul Technical University Scientific Research Projects (ITU BAP) with the project number MYL202243606.

Open access funding is enabled and organized by the Scientific and Technological Research Council of Türkiye, National Academic Network and Information Center (TUBITAK, ULAKBIM).

Conflict of Interest

The authors declare no conflict of interest.

Author Contributions

Burçak Boztemur: Conceptualization (equal); Formal analysis (lead); Investigation (lead); Writing—original draft (equal). **Faruk Kaya:** Investigation (supporting); Software (lead); Writing—review & editing (equal). **Bora Derin:** Software (lead); Writing—review & editing (supporting). **M. Lütfi Öveçoğlu:** Writing—review & editing (equal). **Ju Li:** Formal analysis (supporting); Writing—review & editing (equal). **Duygu Ağaoğulları:** Conceptualization (equal); Project administration (lead); Supervision (lead); Writing—original draft (equal).

Data Availability Statement

The data that support the findings of this study are available from the corresponding author upon reasonable request.

Keywords

magnetic properties, mechanical alloying, mechanochemical syntheses, rare-earth tetraborides

Received: April 6, 2024

Revised: September 5, 2024

Published online: October 3, 2024

- [1] P. K. Liao, K. E. Spear, *J. Phase Equilib.* **1996**, *17*, 326.
- [2] T. Ma, R. Jacobs, J. Booske, D. Morgan, *J. Phys. Chem. C* **2021**, *125*, 17400.
- [3] S. Gabani, K. Flachbart, K. Siemensmeyer, T. Mori, *J. Alloys Compd.* **2020**, *821*, 153201.
- [4] J. Etourneau, P. Hagenmuller, *Philos. Mag. B* **1985**, *52*, 589.
- [5] T. Mori, *J. Phys.: Conf. Ser.* **2009**, *176*, 012036.
- [6] S.-H. Hung, H.-T. Jeng, *Materials* **2020**, *6*, 4381.
- [7] S. Jin, W. Sun, B. Chen, X. Kuang, H. Lu, C. Lu, *J. Phys. Chem. A* **2021**, *125*, 4126.
- [8] P. Tao, J. Ma, S. Li, X. Shao, B. Wang, *Materials* **2023**, *16*, 2627.
- [9] D. Chen, Y. Yang, C. Chen, Y. Meng, Y. Zhang, C. Zhang, *Ceram. Int.* **2023**, *49*, 9862.
- [10] Y. I. Lee, Y. J. Wong, H. W. Chang, W. C. Chang, *J. Magn. Magn. Mater.* **2019**, *478*, 43.
- [11] W. Zhang, B. Zhao, H. Xiang, F. Z. Dai, S. Wu, Y. Zhou, *J. Adv. Ceram.* **2021**, *10*, 62.
- [12] M. Qin, Q. Yan, H. Wang, K. S. Vecchio, J. Luo, *J. Eur. Ceram. Soc.* **2021**, *41*, 2968.
- [13] W. Zhang, B. Zhao, N. Ni, H. Xiang, F. Dai, S. Wu, *J. Mater. Sci. Technol.* **2021**, *87*, 155.
- [14] B. Post, D. Moskowitz, F. W. Glaser, *J. Am. Chem. Soc.* **1956**, *78*, 1800.
- [15] K. E. Spear, *Phase Diagrams*, Springer, Berlin, Heidelberg **1976**, pp. 91–159.
- [16] X. Han, J. Wang, Z. He, *Mod. Phys. Lett. B* **2024**, *38*, 2450179.
- [17] R. Ohlendorf, S. Spachmann, L. Fischer, F. L. Carstens, D. Brunt, G. Balakrishnan, O. A. Petrenko, R. Klingeler, *Phys. Rev. B* **2023**, *108*, 224411.
- [18] V. V. Novikov, A. V. Morozov, A. V. Matovnikov, N. V. Mitroshenkov, D. V. Avdashchenko, S. V. Kuznetsov, B. I. Kornev, O. A. Marakhina, V. V. Novikov, E. O. Bordacheva, *J. Alloys Compd.* **2013**, *581*, 431.
- [19] S. Michimura, A. Shigekawa, F. Iga, M. Sera, T. Takabatake, A. Kikkawa, Y. Tanaka, K. Katsumata, *J. Magn. Magn. Mater.* **2007**, *310*, 2006.
- [20] S. Michimura, A. Shigekawa, F. Iga, M. Sera, T. Takabatake, K. Ohoyama, Y. Okabe, *Phys. B: Condens. Matter.* **2006**, *378*, 596.
- [21] S. Mugiraneza, A. M. Hallas, *Commun. Phys.* **2022**, *5*, 95.
- [22] S. H. Masunaga, V. B. Barbeta, F. Abud, M. S. Torikachvili, R. F. Jardim, *Crystals* **2023**, *13*, 1137.
- [23] D. Brunt, G. Balakrishnan, D. A. Mayoh, M. R. Lees, D. Gorbunov, N. Qureshi, O. A. Petrenko, *Sci. Rep.* **2018**, *8*, 3.
- [24] C. W. Bale, E. Bélisle, P. Chartrand, S. A. Decterov, G. Eriksson, A. E. Gheribi, K. Hack, I. H. Jung, Y. B. Kang, J. Melançon, A. D. Pelton, S. Petersen, C. Robelin, J. Sangster, P. Spencer, M. A. Van Ende, *CALPHAD: Comput. Coupling Phase Diagrams Thermochem.* **2016**, *54*, 35.
- [25] B. Boztemur, M. Mansoor, F. Kaya, M. Huang, E. Tekoğlu, M. L. Öveçoğlu, J. Li, D. Ağaoğulları, *J. Mater. Res. Technol.* **2023**, *24*, 5571.
- [26] C. Suryanarayana, *Prog. Mater. Sci.* **2001**, *46*, 1–184.
- [27] S. Kumar, M. Pownceby, S. Yadav, W. Bruckard, N. Haque, N. Singh, B. Kumar, *Hydrometallurgy* **2024**, *224*, 106249.
- [28] C. Suryanarayana, M. G. Norton, *X-Ray Diffraction: A Practical Approach*, Springer, NewYork, NY **1998**, pp. 3–19.
- [29] D. Ağaoğulları, Ö. Balcı, M. L. Öveçoğlu, C. Suryanarayana, I. Duman, *J. Eur. Ceram. Soc.* **2015**, *35*, 4121.
- [30] D. Ağaoğulları, İ. Duman, M. L. Öveçoğlu, *Ceram. Int.* **2012**, *38*, 6203.
- [31] P. Salamakha, A. P. Gonçalves, O. Sologub, M. Almeida, *J. Alloys Compd.* **2001**, *316*, 5.
- [32] F. Pfeiffer, W. Schafer, G. Will, J. Etourneau, R. Georges, *J. Magn. Magn. Mater.* **1979**, *14*, 306.
- [33] J. Stankiewicz, S. Nakatsuji, Z. Fisk, *Phys. Rev. B: Condens. Matter Mater. Phys.* **2005**, *71*, 134426.
- [34] R. Watanuki, T. Kobayashi, R. Noguchi, K. Suzuki, *J. Phys.: Conf. Ser.* **2009**, *150*, 4.
- [35] G. Will, W. Schafer, F. Pfeiffer, F. Elf, J. Etourneau, *J. Less-Common Met.* **1981**, *82*, 349.
- [36] M. Valeanu, M. Sofronie, A. C. Galca, F. Tolea, M. Elisa, B. Sava, L. Boroica, V. Kuncser, *J. Phys. D: Appl. Phys.* **2016**, *49*, 75001.
- [37] C. C. Zhang, X. Gao, B. Yilmaz, *Catalysts* **2020**, *10*, 1327.
- [38] L. Stoch, M. Środa, *J. Mol. Struct.* **1999**, *511*, 77.
- [39] S. Ram, *Phys. Rev. B* **1995**, *51*, 6280.
- [40] W. A. Pisarski, J. Pisarska, W. Ryba-Romanowski, *J. Mol. Struct.* **2005**, *744*, 515.